

# Crystal Structure and Li-Ion Transport in $\text{Li}_2\text{CoPO}_4\text{F}$ High-Voltage Cathode Material for Li-Ion Batteries

Stanislav S. Fedotov,<sup>\*†,‡,§,||,ID</sup> Artem A. Kabanov,<sup>§</sup> Natalia A. Kabanova,<sup>§</sup> Vladislav A. Blatov,<sup>§,||,ID</sup> Andriy Zhugayevych,<sup>‡,ID</sup> Artem M. Abakumov,<sup>†,‡</sup> Nellie R. Khasanova,<sup>†</sup> and Evgeny V. Antipov<sup>†</sup>

<sup>†</sup>Department of Chemistry, Lomonosov Moscow State University, Moscow 119991, Russia

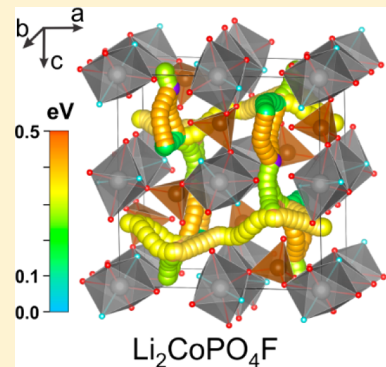
<sup>‡</sup>Skoltech Center for Electrochemical Energy Storage, Skolkovo Institute of Science and Technology, Moscow 143026, Russia

<sup>§</sup>Samara Center for Theoretical Materials Science (SCTMS), Samara University, Samara 443011, Russia

<sup>||</sup>School of Materials Science and Engineering, Northwestern Polytechnical University, Xi'an, Shaanxi 710072, People's Republic of China

## Supporting Information

**ABSTRACT:** In this work, we provide a structural and computational investigation of the  $\text{Li}_2\text{CoPO}_4\text{F}$  high-voltage cathode material by means of neutron powder diffraction (SG  $Pnma$ ,  $a = 10.4528(2)$  Å,  $b = 6.38667(10)$  Å,  $c = 10.8764(2)$  Å,  $R_F = 0.0145$ ), crystal chemistry approaches (Voronoi–Dirichlet partitioning and bond valence sums mapping), and density functional theory. The material reveals low energy barriers (0.12–0.43 eV) of Li hopping and a possible 3D channel system for Li-ion migration. It is found that only one Li per formula unit can be extracted within the potential stability window of the commercially available electrolytes. The interrelation between dimensionality, topology and energetics of Li-ion diffusion and peculiarities of the  $\text{Li}_2\text{CoPO}_4\text{F}$  crystal structure are discussed in detail.



## INTRODUCTION

The progress in Li-ion batteries (LIB) is largely governed on the development of new materials capable of meeting rigorous demands of new emerging applications. Specific energy, the key parameter for LIB's performance, critically depends on the properties of the electrode materials, in particular, cathode materials. Cathode is the primary component not only influencing the operating voltage of a Li-ion battery but also defining practical capacity. Discovery and subsequent deployment of the  $\text{LiFePO}_4$  cathode material<sup>1</sup> attracted wide interest to polyanion-type compounds, which were a subject of very intensive research in the last two decades. Despite the smaller theoretical gravimetric capacity compared to that of the layered oxides due to the presence of polyanion groups, the inherent advantages of polyanion-type materials are indisputable. Their stable framework supports long-term structural stability, which is essential for extensive cycling and safety issues. The chemical nature of the polyanion group  $(\text{XO}_z)^{m-}$  allows tuning the  $\text{M}^{(n+1)+}/\text{M}^{n+}$  redox potential through the inductive effect, resulting in a higher operating voltage compared to that in the oxide materials.<sup>2,3</sup> Further advancement in polyanion materials has been achieved by combining  $(\text{XO}_4)^{m-}$  ( $\text{X} = \text{S}$  or  $\text{P}$ ) and  $\text{F}^-$  ions. Here, the increase in the working potential is due to higher ionicity of the  $\text{M}-\text{F}$  bond, whereas faster kinetics stems from the lower affinity of lithium to the  $\text{F}^-$  anion. Moreover, incorporation of different species into the anion

sublattice results in a variety of polyanion crystal structures, increasing considerably a number of potential candidates.

Among fluoride–phosphates,  $\text{Li}_2\text{MPO}_4\text{F}$  ( $\text{M} = \text{Fe}, \text{Mn}, \text{Co}$ ,  $\text{Ni}$ ) compounds have attracted special attention as promising high-energy cathode materials, because of the high specific capacity ( $\sim 280$  mAh/g) expected for an exchange of two alkali ions per formula unit.<sup>4–7</sup> These compounds possess different crystal structures depending on the transition metal.<sup>8–10</sup>  $\text{Li}_2\text{CoPO}_4\text{F}$  with a 3D framework structure exhibits reversible electrochemical activity at high operating voltages (above 5 V). Various synthetic techniques resulted in  $\text{Li}_2\text{CoPO}_4\text{F}$  delivering discharge capacities of 80–110 mAh/g with rather poor cycling performance explained by high operating potentials and the absence of stable electrolytes working at these potentials.<sup>6,11–14</sup> This problem was partly solved by coating material's particles and switching to a high-voltage electrolyte that considerably suppresses the effect of side reactions at high potentials and enhances the discharge capacity up to 140 mAh/g.<sup>15–19</sup> Furthermore, the specific capacity close to the theoretical value (144 mAh/g, one  $\text{Li}^+$  cation) was achieved for a full cell consisting of the  $\text{Li}_3\text{PO}_4$ -coated  $\text{Li}_2\text{CoPO}_4\text{F}$  cathode and  $\text{TiO}_2$  anode.<sup>20</sup> However, in spite of extensive studies, a possibility of de/intercalation of higher amounts of lithium in this material

Received: November 2, 2016

Revised: January 17, 2017

Published: January 20, 2017

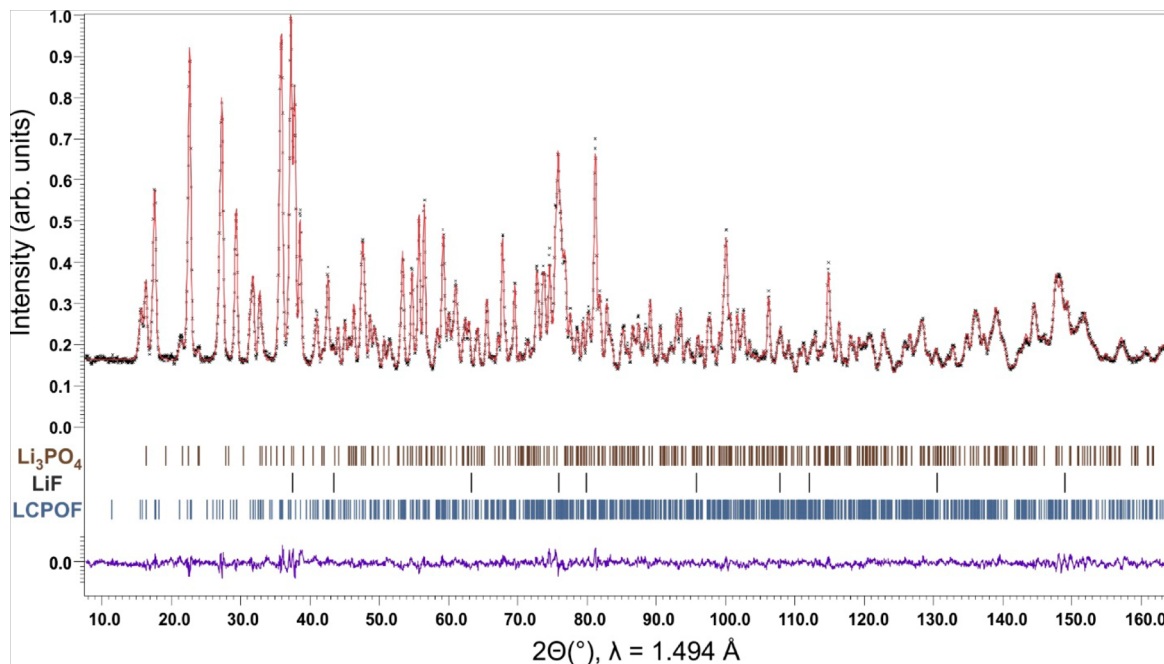


**Figure 1.** Experimental, calculated, and difference NPD profiles after the Rietveld refinement of  $\text{Li}_2\text{CoPO}_4\text{F}$ . The bars designate the reflection positions of the  $\text{LiF}$  ( $Fm\bar{3}m$ ,  $a = 4.0281(2)$  Å,  $V = 65.356(5)$  Å $^3$ ,  $R_F = 0.0107$ ) and  $\text{Li}_3\text{PO}_4$  ( $Pnma$ ,  $a = 10.467(3)$  Å,  $b = 6.117(2)$  Å,  $c = 4.931(1)$  Å,  $V = 315.69(2)$  Å $^3$ ,  $R_F = 0.0146$ ) impurities, and  $\text{Li}_2\text{CoPO}_4\text{F}$  main phase (indicated as LCPOF;  $Pnma$ ,  $a = 10.4528(2)$  Å,  $b = 6.38667(10)$  Å,  $c = 10.8764(2)$  Å,  $V = 726.10(2)$  Å $^3$ ,  $R_F = 0.0145$ ,  $R_p = 0.0257$ ,  $R_{wp} = 0.0321$ , GOF = 1.76).

**Table 1. Fractional Atomic Coordinates, Atomic Displacement Parameters for  $\text{Li}_2\text{CoPO}_4\text{F}$**

atom	position	$x/a$	$y/b$	$z/c$	$U_{iso}$ , Å $^2$
Li1	8d	0.7590(8)	0.9845(11)	0.6627(7)	0.029(2)
Li2	4c	0.9719(9)	0.75	0.7244(8)	0.017(2)
Li3	4c	0.2686(11)	0.25	0.5822(9)	0.014(2)
Co1	4a	0	0	0	0.0104(12)
Co2	4b	0	0	0.5	0.0096(12)
P1	4c	0.7561(3)	0.75	0.9204(2)	0.0065(5)
P2	4c	0.0219(3)	0.25	0.7422(3)	0.0068(6)
O1	8d	0.8104(2)	0.9461(3)	0.9839(2)	0.0081(3)
O2	4c	0.6101(2)	0.75	0.9432(2)	0.0093(5)
O3	4c	0.7832(3)	0.75	0.7841(2)	0.0101(6)
O4	8d	-0.03317(15)	0.4453(3)	0.6797(2)	0.0100(4)
O5	4c	0.1697(2)	0.25	0.7433(3)	0.0125(5)
O6	4c	-0.0264(3)	0.25	0.8797(3)	0.0069(5)
F1	4c	0.0578(3)	0.75	0.8798(3)	0.0112(6)
F2	4c	0.8650(3)	0.75	0.5332(2)	0.0104(5)

remains unclear. To evaluate the electrochemical activity of  $\text{Li}_2\text{CoPO}_4\text{F}$ , various computational methods have actively been used to obtain information on diffusion paths and activation energies of the Li-ion transport. Among them, molecular dynamics (MD) simulations supported two different conjectures: either 1D Li-ion migration pathways<sup>15</sup> or a 3D Li-ion diffusion network forecasting good Li-ion conductivity.<sup>21</sup> Those calculations were carried out with the structural models obtained from either synchrotron powder data (SXPD)<sup>15</sup> or precession electron diffraction (PED).<sup>22</sup> Although both models are reliable, the precision in the Li positions might be insufficient due to low sensitivity of X-ray and electron diffraction to such light elements as Li. In this paper, we present the investigation of Li-ion transport properties of  $\text{Li}_2\text{CoPO}_4\text{F}$  using a combined approach comprising crystal chemistry (Voronoi–Dirichlet partition, VDP, and bond

valence summation, BVS) and density functional theory nudged elastic bands (DFT-NEB) methods. The computational analysis is based on the crystal structure refined from neutron powder diffraction data with accurately determined positions of Li atoms.

## EXPERIMENTAL SECTION

**Sample Preparation.** About 4 g of  $\text{Li}_2\text{CoPO}_4\text{F}$  powder was prepared via a two-step solid-state reaction. At first,  $\text{LiCoPO}_4$  was synthesized using a freeze-drying technique. Stoichiometric amounts of  $\text{Co}(\text{NO}_3)_2 \cdot 6\text{H}_2\text{O}$  (99%, Labteh) and  $\text{LiH}_2\text{PO}_4$  (99.9%, Sigma-Aldrich) were dissolved in distilled water to form a clear pink solution, which was dispersed into liquid nitrogen under constant stirring. The resulting cryogranulated powder was put into a vacuum sublimation machine (Labconco Freezone 7948030) and dried at the pressure of 0.1–0.3 mbar

and gradually rising temperature from  $-40$  to  $+20$  °C during 72 h. The resulting powder was annealed at 380 °C for 10 h to remove all volatile components and then grinded in the ball-milling machine (Fritsch Pulverisette, 160 rpm, 2 h, acetone media) and fired at 600 °C under an argon flow for 10 h to get the final product.

The obtained LiCoPO<sub>4</sub> was mixed with 3% excess of LiF (99.9%, Vekton) by ball milling, pressed into pellets, and annealed under an argon flow at 670 °C for 1 h with subsequent quenching at the same atmosphere to room temperature.

**Structure Refinement.** Neutron powder diffraction (NPD) data were collected on the high-resolution powder diffractometer, HRPT (Paul Scherrer Institute (PSI), Switzerland), at the wavelength of 1.494 Å. The Rietveld refinement of the Li<sub>2</sub>CoPO<sub>4</sub>F structure was performed using JANA2006 program package.<sup>23</sup> The cell parameters (SG no. 62 *Pnma*) and fractional coordinates from the single crystal X-ray diffraction experiment on the isostructural Li<sub>2</sub>NiPO<sub>4</sub>F<sup>8</sup> phase served as a starting model. A careful inspection of NPD data revealed the presence of minor impurities of LiF and Li<sub>3</sub>PO<sub>4</sub>, which were included into the refinement, and their amounts were found to be 1.6 and 3.5 wt %, respectively (Figure 1). The refinement led to full occupancies for all sites. The experimental, calculated, and difference NPD profiles after the Rietveld refinement are shown in Figure 1. The atomic positions are provided in Table 1; the interatomic distances are summarized in Table 2. The labels for the atomic positions and the atomic coordinates are brought into accordance with those reported by Hadermann et al.<sup>22</sup>

**Table 2. Selected Interatomic Distances for Li<sub>2</sub>CoPO<sub>4</sub>F**

bond	distance, Å	bond	distance, Å
Li1–O1	2.126(8)	Co1–O1	2.019(2) $\times$ 2
Li1–O3	2.013(8)	Co1–O6	2.086(2) $\times$ 2
Li1–O4	2.225(8)	Co1–F1	2.152(2) $\times$ 2
Li1–O5	2.190(7)	Co2–O2	2.063(2) $\times$ 2
Li1–F2	2.336(8)	Co2–O4	2.015(2) $\times$ 2
Li2–O2	2.327(10)	Co2–F2	2.161(2) $\times$ 2
Li2–O3	2.073(10)	P1–O1	1.538(2) $\times$ 2
Li2–O4	2.004(3) $\times$ 2	P1–O2	1.543(4)
Li2–F1	1.913(10)	P1–O3	1.513(4)
Li2–F2	2.361(10)	P2–O4	1.537(2) $\times$ 2
Li3–O1	2.117(4) $\times$ 2	P2–O5	1.541(4)
Li3–O5	2.026(9)	P2–O6	1.573(4)
Li3–O6	2.199(10)		
Li3–F2	1.866(10)		

**FTIR.** Fourier transform infrared (FTIR) spectra (650–4000 cm<sup>-1</sup> region) were acquired using an Agilent Carry 630 FTIR apparatus equipped with an attenuated total reflectance (ATR) accessory.

## ■ COMPUTATIONAL DETAILS

**VDP.** The Voronoi–Dirichlet partitioning (VDP) analysis was performed in ToposPro program.<sup>24</sup> The procedure of the analysis is described in detail in our previous works.<sup>14,25</sup> The significant, i.e., available for the Li<sup>+</sup> cations, voids, and channels were selected applying the following geometry criteria:  $R_{SD} > 1.3$  Å,  $R_{ch} > 1.8$  Å, where  $R_{SD}$  is the radius of the void and  $R_{ch}$  is the radius of the channel ( $R_{ch} = R_{Li} + \langle R_{anion} \rangle$ ).<sup>26</sup>

**BVS.** Suitable sites for mobile ions in a crystal structure can be localized using empirically established relationships between the bond length,  $R$ , and a so-called bond valence,<sup>27</sup>  $s$ , defined by the following formula:

$$s_{A-X} = e^{R-R_0/b}$$

The sites are determined as regions of the structure, where a bond valence sum, BVS =  $\sum s_{A-X}$ , over all adjacent counterions X approaches an “ideal valence”, BVS<sub>Id</sub>, which is the absolute value of its oxidation state (1 in the case of Li).

In the field of ionic conductors, bond valence landscapes are used to determine and directly visualize mobile ion diffusion pathways. The procedure comprises the subdivision of a unit cell with a given step (0.2 Å in this work), automated calculation of the BVS value in each section and, finally, construction of a three-dimensional map mainly characterized by a so-called BV cutoff (or mismatch) value,  $\Delta BVS = BVS - BVS_{Id}$ , which confines the deviation of the BVS values from the reference value (1 for Li). The more the deviation in a particular area, the lower the possibility for Li<sup>+</sup> to move through this area. Typically, the  $\Delta BVS$  values for a mobile ion should not exceed 10–15% of its formal oxidation state (reference value). This approach is competently implemented in the 3DBVSMPER program as the bond valence sums mapping (BVSM) script<sup>28</sup> utilized in this work. In contrast to the VDP approach, the BVS methods take into account not only geometry parameters of the particular structure but also charge interactions between a mobile ion (Li<sup>+</sup>) and framework anions. As a result, a migration map produced by BVS methods is shaped by both geometric and electrostatic parameters of the ion diffusion. Another advantage of the BV methods over VDP is a much higher spatial resolution. In the case of the VDP approach, a migration path necessarily goes through the barycenters of discrete significant voids linked by significant channels, with their physical contours being disregarded. Thus, such an arrangement outlines only a general view on the diffusion system and its dimensionality. On the contrary, the BVS method produces more detailed 3D contours of the crystal space volume acceptable for migration taking into account both geometric and electrostatic considerations.

**DFT-NEB.** The activation energy barriers for Li<sub>2</sub>CoPO<sub>4</sub>F were calculated using DFT-NEB method<sup>29,30</sup> based on the generalized gradient approximation (GGA) with the Perdew–Burke–Ernzerhof (PBE) functional<sup>31</sup> and projector augmented wave (PAW) pseudopotentials<sup>32</sup> as implemented in the Vienna ab initio simulation package, VASP.<sup>33</sup> The Monkhorst–Pack 4  $\times$  4  $\times$  4  $k$ -point grid was utilized and the cutoff energy was fixed to 600 eV in all calculations. For the geometry optimization, the convergence thresholds for the total energy and force components were chosen as 10<sup>-6</sup> eV and 10<sup>-5</sup> eV/Å, respectively. A further increase of the cutoff energy or  $k$  grid leads to negligible changes in the results. All the NEB calculations were performed in a 1  $\times$  2  $\times$  1 supercell ( $a = 10.288$  Å,  $b = 12.810$  Å,  $c = 10.688$  Å,  $V = 1408.56$  Å<sup>3</sup>) with Li<sub>32</sub>Co<sub>16</sub>P<sub>16</sub>O<sub>64</sub>F<sub>16</sub> stoichiometry without the Hubbard  $U$  correction, whose absence had a minor effect on the calculated activation energies for similar compounds such as LiVPO<sub>4</sub>F and LiFeSO<sub>4</sub>F.<sup>34</sup> The shape and volume of the supercell were kept fixed at the optimized geometry. For the visualization of DFT-NEB Li migration pathways VESTA software was used.<sup>35</sup>

**Average Voltage Profile.** The average electrode potential is calculated as

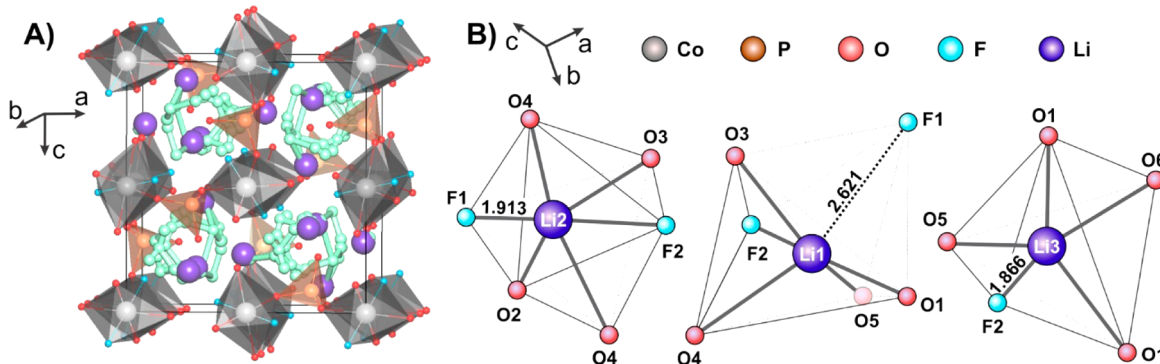


**Figure 2.** (A) Ball-polyhedral representation of the  $\text{Li}_2\text{CoPO}_4\text{F}$  crystal structure with the VDP produced system of voids and channels (light-green spheres and cylinders). (B) Coordination polyhedra for  $\text{Li}^+$  (octahedron),  $\text{Li}^+$  (square pyramid/distorted octahedron), and  $\text{Li}^+$  (square pyramid).

$$\text{eV} = (E(x_1) - E(x_2))/(x_1 - x_2) - E(\text{Li})$$

where  $E(x)$  is the energy of  $\text{Li}_{2-x}\text{CoPO}_4\text{F}$  per formula unit and  $E(\text{Li})$  is the per-atom energy of the crystalline Li. The calculations were performed for  $x = 0, 1, 1.5$ , and  $2$ . The GGA +U method was used.<sup>36,37</sup> The  $U$  value for Co was set to  $5.7$  eV, which fitted best the experimental data for Co-containing materials studied in ref 38. The energy cutoff was set to  $400$  eV. The  $\Gamma$ -centered Monkhorst-Pack  $3 \times 5 \times 3$   $k$ -grid was taken for energy optimization, whereas the  $9 \times 15 \times 9$   $k$ -grid was used in single point calculations. Gaussian smearing with  $0.05$  eV width was applied for orbital population in energy minimization, whereas tetrahedron method with Blöchl corrections was used for single point calculations. Initial spin ordering was assumed to be ferromagnetic in all the calculations. Equilibrium lattice geometry was obtained by fourth-order polynomial fit of energy for a set of fixed-volume relaxations (Figure S1 of Supporting Info).

## RESULTS AND DISCUSSION

The crystal structure of  $\text{Li}_2\text{CoPO}_4\text{F}$  is shown in Figure 2. Rutile-like chains of distorted edge-shared  $\text{CoO}_4\text{F}_2$  octahedra running along the  $b$ -axis are linked to each other through  $\text{PO}_4$  tetrahedral groups to generate a robust 3D polyhedral framework with voids and channels where lithium atoms are located. Two crystallographically distinguishable cobalt sites represent the  $\text{CoO}_4\text{F}_2$  octahedra hosting fluorine atoms in *trans*-configuration, with the Co–F distances being longer than the Co–O ones.

Three distinct fully occupied lithium positions coordinated by O and F atoms were found (Figure 3). The Li1 site is surrounded by four oxygen and one fluorine atoms at the vertices of a square pyramid, the fluorine atom is situated at the basal vertex with a rather long Li1–F2 distance ( $2.336$  Å). The nearest F1 atom, located at  $2.621$  Å, can also contribute to the Li1 environment resulting in the  $[5 + 1]$  coordination of the Li1 site. The Li2 atom is octahedrally coordinated by four oxygen and two fluorine atoms. The fluorine atoms occupy two axial positions forming the shortest ( $1.913$  Å) and the longest ( $2.361$  Å) bonds within the Li2–X bond distances. The coordination environment of the Li3 atom comprises four oxygen and one fluorine atoms, where the Li3–F2 distance is the shortest in its coordination sphere ( $1.866$  Å).

To investigate the possibility of the F/OH mixing in  $\text{Li}_2\text{CoPO}_4\text{F}$ , the FTIR spectroscopy analysis was carried out. No distinctive bands in the  $2500$ – $4000$   $\text{cm}^{-1}$  region were evidenced (Figure 3) validating the absence of both –OH

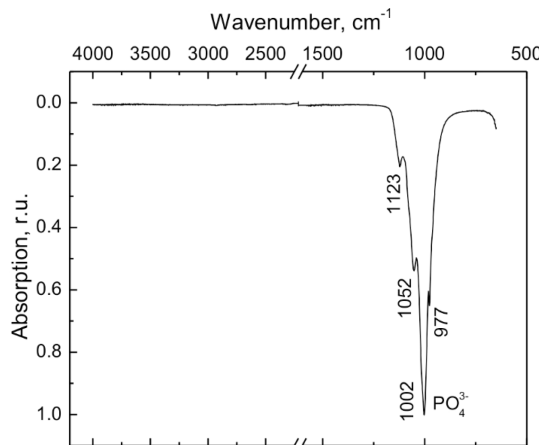


**Figure 3.** FTIR spectrum of  $\text{Li}_2\text{CoPO}_4\text{F}$ .

groups and adsorbed water. A group of bands within the  $950$ – $1150 \text{ cm}^{-1}$  range is attributed to the  $\text{PO}_4$  asymmetric stretch mode.

The mobility and structural accessibility of the Li atoms in the framework are known to determine largely electrochemical performance of the cathode materials. Thus, a comprehensive understanding of the ion transport provides a tool to improve practical battery performance through a proper tuning of the electrode material morphology. Moreover, it becomes essential when considering materials for high-power applications. Thus, a careful analysis of the Li-ion transport system in  $\text{Li}_2\text{CoPO}_4\text{F}$  was performed.

The VDP approach provides a quick tentative insight in the Li-ion migration. According to the VDP analysis (Figures 2A and 4, top), the space available for Li atoms in  $\text{Li}_2\text{CoPO}_4\text{F}$  comprises three nonequivalent continuous sets of significant voids and channels, which correspond to three transitions between the Li positions (Figure 2A, Figure 4, paths 1–3). These transitions form 1D chain-like migration pathways along the  $[010]$  direction involving all three Li sites (Figure 2A, Figure 4, top). The largest voids and channels are found in the vicinity of the Li1 and Li3 sites. Both Li1 and Li3, located near the large basal planes of the corresponding  $\text{LiO}_4\text{F}$  square pyramids, possess more spacious coordination environments in contrast to the Li2 site positioned in the center of an almost regular octahedron, which confines the accessible space for Li. Still, there are definitely no Li sites, which would be trapped in the framework or somehow hindered sterically.

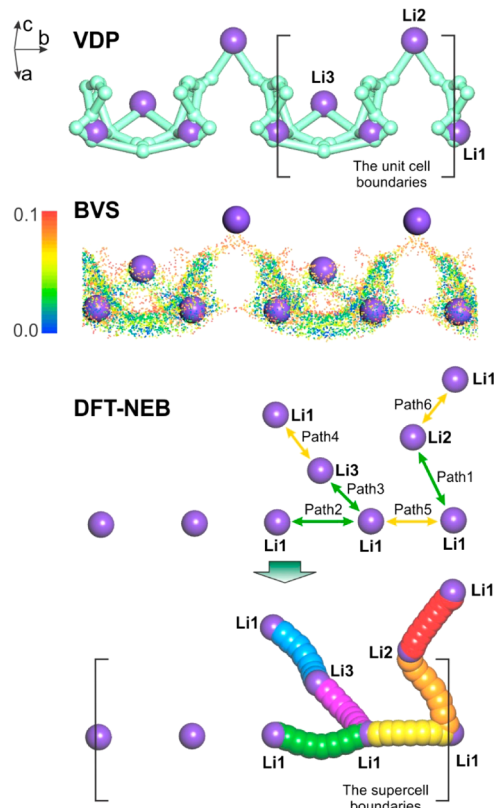


**Figure 4.** Top: Li-ion migration pathways obtained by VDP ( $R_{SD} = 1.3 \text{ \AA}$ ,  $R_{ch} = 1.8 \text{ \AA}$ ) and BVS ( $\Delta BVS = 0.1 \text{ vu}$ ). Light-green spheres and cylinders represent significant voids and channels, respectively. The magnitude of the BVS deviation is scaled in a reverse-rainbow manner, ranging from dark blue ( $\Delta BVS = 0.0$ ) to red ( $\Delta BVS = \pm 0.1$ ). Bottom: paths 1–6 according to the DFT-NEB calculations. The green arrows designate the transitions favored by the VDP and BVS analyses, the yellow arrows describe the additionally considered neighboring Li–Li transitions.

The BVS mapping for  $\text{Li}_2\text{CoPO}_4\text{F}$  results in a similar pattern of the Li transport system, which consists of [010] one-dimensional pathways exhibiting almost the same profile produced by VDP (Figure 4, top). The Li1 and Li3 atoms are accommodated in the quite spacious channels and the Li2 atoms are separated by much narrower ones. Remarkably, there is an obvious discrepancy between two symmetry inequivalent  $\text{Li1} \leftrightarrow \text{Li1}$  transitions: the first one is characterized by low  $\Delta BVS$  values, and the other, by high  $\Delta BVS$  values, being almost inaccessible, which was also confirmed by VDP. Eventually, the BVS method at the given  $\Delta BVS$  (0.1 vu) well reproduces the VDP results identifying no alternative paths.

Despite some advantages of BVS over VDP, both methods still deal with a static model of the crystal structure, not considering possible lattice distortions or atoms displacements during the ion migration. These “crystal chemistry” methods provide a tentative view on the Li-ion migration pattern within the structure, consequently being used for the fast preliminary analysis. However, the Li migration maps obtained by VDP or BVS are usually in fairly good agreement with the experimental data or much sophisticated simulations such as molecular dynamics or density functional theory.<sup>39,40</sup>

The Li-ion transport system was further investigated by the DFT-NEB method. The accessible transitions between the Li sites retrieved from the VDP and BVS analyses (paths 1–3)

were taken as starting conditions for the DFT-NEB simulations. Additionally, three other close transitions (path 4–6, Figure 4, bottom) were also considered despite their inaccessibility for  $\text{Li}^+$  ions within the static structure model (Figure 2, Table 3).

**Table 3. Activation Energies and Migration Path Lengths in  $\text{Li}_2\text{CoPO}_4\text{F}$  According to DFT-NEB**

path no.	path length, Å	transition type	$E_a$ , eV
1	3.677	$\text{Li1} \leftrightarrow \text{Li2}$	0.35
2	3.330	$\text{Li1} \leftrightarrow \text{Li1}$	0.12
3	3.130	$\text{Li3} \leftrightarrow \text{Li1}$	0.43
4	3.110	$\text{Li3} \leftrightarrow \text{Li1}$	0.34
5	3.167	$\text{Li1} \leftrightarrow \text{Li1}$	0.41
6	2.416	$\text{Li1} \leftrightarrow \text{Li2}$	0.37

The calculated energy profiles along paths 1–6 are presented in Figure 5. By an energy barrier of nonequivalent Li transitions (paths 1, 3, 4, 6) we will further imply the highest activation energy of the Li hopping along the both directions. For instance, the energy barrier corresponding to the  $\text{Li1} \leftrightarrow \text{Li2}$  transition along path 1, reaches 0.35 eV. Such asymmetrical energy profiles for the nonequivalent Li transitions (paths 1, 3, 4, 6) exhibit obvious thermodynamic differences between Li hopping in the opposite directions. All the activation energy values of the Li hopping are summarized in Table 3.

Interestingly, paths 4–6, which are not suitable for Li-ion migration from the crystal chemistry analysis, are characterized by quite ordinary energy barriers varying from 0.34 to 0.41 eV (Table 3). The reason is that the VDP and BVS methods based on the static structure model cannot take into account large framework distortions during the migration of cations. At the same time, our modeling of the lattice relaxation during  $\text{Li}^+$  migration through, for instance, path 6 showed that the channel diameter increases by almost 0.3 Å due to extending of the O3–O4 edge. In general, this means that the geometry analysis could be insufficient for prediction of migration via channels, which are comparable by length with significant (wide) channels but have radii smaller than the accepted  $R_{ch}$  threshold. Such channels should be also included into the NEB analysis. However, when dealing with a rigid framework, which is not subjected to a severe volume variation upon Li de/intercalation, the crystal chemistry methods certainly score against the DFT computations in time costs, resulting in a reliable Li-ion migration map.

The other peculiarity can be seen in almost a 4-fold difference between the energy barriers of the two symmetry inequivalent  $\text{Li1} \leftrightarrow \text{Li1}$  transitions (path 2, 0.12 eV and path 5, 0.41 eV). The reason probably lies in the neighboring terminal O3 and O5 atoms of  $\text{P}_1\text{O}_4$  and  $\text{P}_2\text{O}_4$  tetrahedra, respectively, which are both directed toward the center of the channels. Such “dangling” O atoms, which are not coordinated by other framework atoms except for P, normally have extra electron density on them in comparison to the O atoms shared by both  $\text{CoO}_4\text{F}_2$  and  $\text{PO}_4$  polyhedra. This electron density/negative charge can be redistributed/compensated only by forming ionic bonds with  $\text{Li}^+$  cations. Thus, the Li1 atoms in their coordination environments should be more strongly bonded with the O3 and O5 atoms than to the rest of the oxygen atoms. Next, the  $\text{Li1}-\text{O}3$  interatomic distance turns out to be shorter than the  $\text{Li1}-\text{O}5$  one by roughly 0.2 Å (Figure 6), thus requiring more energy to break the bond and bringing about a higher energy barrier of Li migration near the O3 atom.

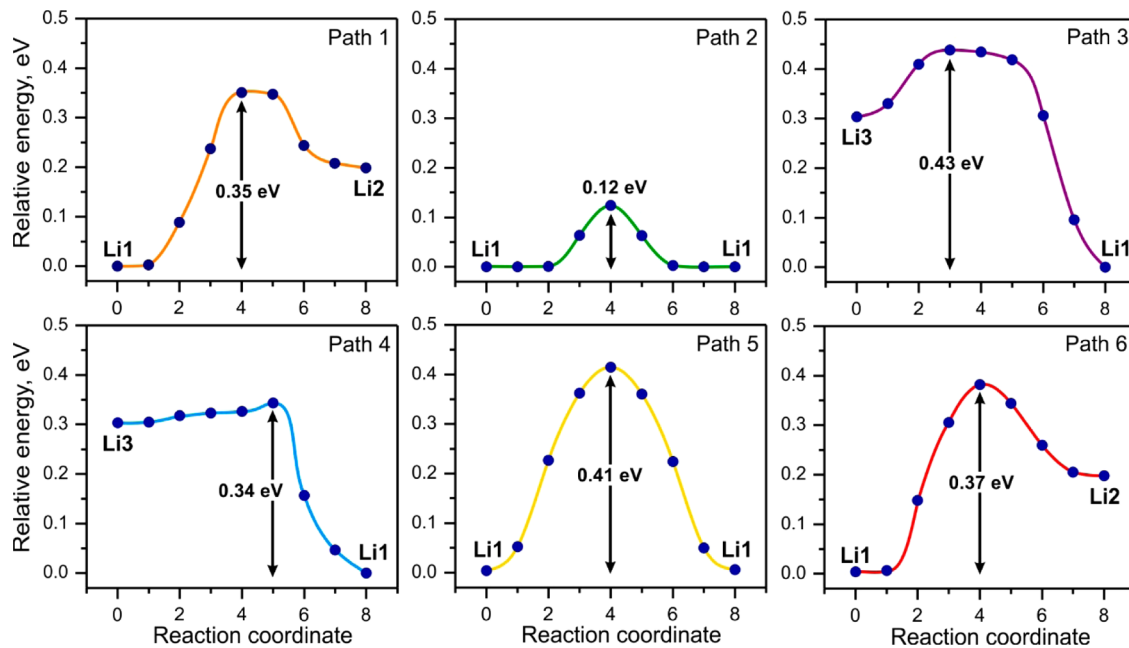


**Figure 5.** Calculated energy profiles for the investigated Li transitions in  $\text{Li}_2\text{CoPO}_4\text{F}$ . Calculations are performed at a high concentration of Li ( $(\text{Li}_{31}\text{Co}_{16}\text{P}_{16}\text{O}_{64}\text{F}_{16})$  stoichiometry). Li1,2,3 labels designate the position of Li vacancies. For instance, the migration of the Li vacancy along path 1 is characterized by the following equation:  $V_{\text{Li}1} + V_{\text{Li}2}^X \rightarrow V_{\text{Li}2} + V_{\text{Li}1}^X$ .

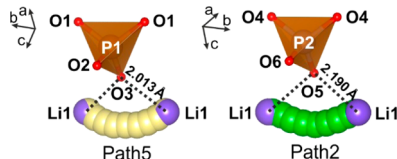


**Figure 6.** Schematic ball-polyhedral representation of the Li migration around the “dangling” O3 and O5 atoms of the corresponding PO<sub>4</sub> groups.

Consequently, six Li migration paths representing the six possible neighboring transitions between three crystallographic positions of lithium (Figure 2) produce a 3D Li-ion migration map displaying quite low values of energy barriers (0.12–0.43 eV). Importantly, all three Li sites corresponding to two Li atoms per  $\text{Li}_2\text{CoPO}_4\text{F}$  can participate in the 3D Li diffusion process (Figure 7), which is more favorable than 1D or 2D diffusion for attaining high-power characteristics. These results are consistent with the atomistic simulations by Lee et al.<sup>21</sup> supporting the possibility of the 3D Li migration.

Regardless of the dimensionality, the Li-ion diffusion process in both above-mentioned scenarios comprises all Li atoms in three Li sites, which correspond to two Li equivalents per

formula. Still, to the best of our knowledge, there is no reliable data in the literature verifying the extraction of more than one Li equivalent from  $\text{Li}_2\text{CoPO}_4\text{F}$ . In addition to the energy barriers, the readiness of Li de/intercalation is largely determined by the electrode potential of the  $\text{Co}^{(n+1)+}/\text{n}^+$  redox transitions ( $n = 2, 3$ ). In the case of  $\text{Li}_2\text{CoPO}_4\text{F}$ , the potentials attributed to the extraction of the second Li atom supposedly belong to a high-voltage domain (over 5 V). Unfortunately, experimental investigation of the material performance at such voltages is drastically impeded by severe electrolyte decomposition. To estimate the electrode potentials associated with various amounts of extracted Li, we used GGA+U based DFT simulations.

Because reliable structure data are available only for the pristine  $\text{Li}_2\text{CoPO}_4\text{F}$ , the initial geometries of partially and fully deintercalated states ( $\text{Li}_{2-x}\text{CoPO}_4\text{F}$ ,  $x = 1, 1.5, 2$ ) for DFT simulations were created manually from the parent  $\text{Li}_2\text{CoPO}_4\text{F}$  on the basis of a model of the ordered Li extraction. According to this model, the Li1 site is likely to be depleted first as revealed by the XRD<sup>6</sup> and Li NMR data,<sup>15</sup> with a subsequent removal of (a) Li2 ( $x = 1.5$ ) and then Li3 ( $x = 2$ ) sites or vice versa (b) Li3 ( $x = 1.5$ ) and Li2 ( $x = 2$ ). The preferable Li deintercalation from the Li1 position is also supported by the calculations of Li vacancy formation energies within the parent structure: for Li1 (2.309 eV) it was found to be 0.2–0.3 eV lower than for Li2 and Li3 (2.517 and 2.602 eV, respectively). The initial unit cell parameters for  $x = 1$  were taken the same as for the electrochemically oxidized  $\text{Li}_{1+\beta}\text{CoPO}_4\text{F}$  refined from the XRD data,<sup>6</sup> the optimization of the unit cell parameters for  $x = 1.5, 2$  was started from those for  $x = 1$ .

The calculated unit cell parameters of  $\text{Li}_{2-x}\text{CoPO}_4\text{F}$  are summarized in Table 4. Upon subsequent Li removal, the unit cell does not experience significant volume variation, evidencing the stability of the polyhedral framework. Supposedly, there are two simultaneous competing processes taking place during the Li deintercalation, which influence the volume change: shrinkage due to decreasing the  $\text{Co}^{n+}$  ( $n > 2$ )

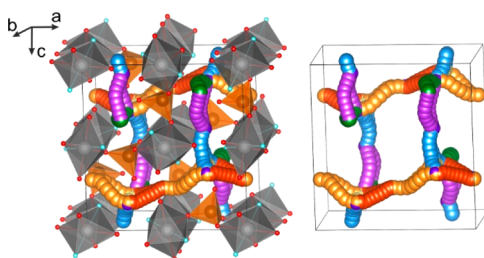


**Figure 7.** DFT-NEB results: Li migration system in  $\text{Li}_2\text{CoPO}_4\text{F}$  consisting of paths 1–6. Co atoms are designated as gray, phosphorus as orange, and oxygen and fluorine as red and blue spheres.

**Table 4. Experimental and Calculated (GGA+U) Unit Cell Parameters of  $\text{Li}_{2-x}\text{CoPO}_4\text{F}$  ( $x = 0, 1, 1.5, 2$ )**

$x$ in $\text{Li}_{2-x}\text{CoPO}_4\text{F}$		$a$ , Å	$b$ , Å	$c$ , Å	$V$ , Å <sup>3</sup>
0	exp	10.4528(2)	6.38667(10)	10.8764(2)	726.10(2)
	calc	10.5657	6.4465	10.9873	748.37
1	exp	10.855(5)	6.271(2)	11.018(6)	750.0(8)
	calc	10.9405	6.2413	11.2189	766.05
1.5	calc (a) Li <sub>2</sub>	10.9602	6.2512	10.8970	746.60
	calc (b) Li <sub>3</sub>	10.8636	6.2060	11.0452	744.66
2	calc	10.9933	6.2224	11.0456	755.57

ionic radius compared to that of  $\text{Co}^{2+}$  and expansion owing to the Coulomb repulsion of the oxygen and fluorine anions with the subsequent polyhedral rotation. As a result, an expansion of 4.1% with respect to the initial material can be witnessed, which is a much smaller volume variation in comparison to cases of other Li-containing phosphates and fluoride–phosphates ( $\text{LiFePO}_4$ , 6.8%;<sup>41</sup>  $\text{LiVPO}_4\text{F}$ , 8.5%).<sup>42</sup>

The obtained values of the electrode potentials depending on Li content are presented in Figure 8. Indeed, the removal of the

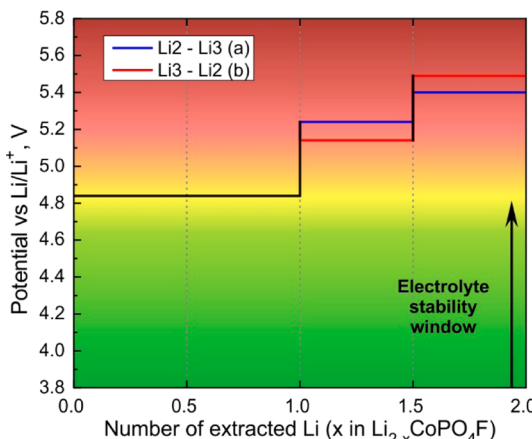


**Figure 8.** Calculated voltage profile for  $\text{Li}_2\text{CoPO}_4\text{F}$ .

first Li atom is characterized by an electrode potential centered at 4.84 V vs  $\text{Li}/\text{Li}^+$  (Figure 8) that is fairly close to the experimentally observed values of 4.8–4.9 V.<sup>12,16,18</sup> Nevertheless, this potential is located at the edge of the stability window of most of conventional electrolytes. Typically, it requires utilizing specific additives,<sup>15,18</sup> which improve the electrolyte stability, and/or protective coatings<sup>16,17</sup> to entirely fulfill the de/intercalation of one Li. Further, an increase of the potential to 5.24 or 5.14 V (for Li2 (a) or Li3 (b), respectively) corresponding to the extraction of half of the second Li atom, can be observed. The extraction of the remaining 0.5 Li equivalent should occur at much higher potentials of 5.40 or 5.49 V (for Li3 (a) and Li2 (b), respectively) at which oxygen oxidation might occur. The latter assumption is in good agreement with the results of detailed analysis of the pDOS for  $\text{Li}_{2-x}\text{CoPO}_4\text{F}$  (Figure S2 of Supporting Info), which clearly shows increasing oxygen pDOS near the Fermi level, with  $x$  indicating that the deintercalated materials should have pronounced tendency to the oxygen oxidation starting from  $x = 1$  and progressing at higher  $x$ . At the same time,  $\text{Li}_{2-x}\text{CoPO}_4\text{F}$  can be subjected to a Li/Co antisite disorder, which was recently observed for iron in the isostructural  $\text{Li}_2\text{FePO}_4\text{F}$ .<sup>43</sup>

Despite the fact that according to the NEB simulations, all three Li sites can be involved into the migration processes, the computed electrode potentials, which are far beyond the electrolyte stability window, clearly demonstrate that the de/intercalation of the second Li equivalent can be hardly achieved due to hindrances with the electrolyte degradation and/or anion sublattice oxidation.

## CONCLUSIONS

$\text{Li}_2\text{CoPO}_4\text{F}$  fluoride phosphate cathode material was successfully synthesized using a freeze-drying-assisted solid-state approach. Its crystal structure was refined on the basis of neutron diffraction data allowing for reliable determination of the positions of Li atoms. A combined VDP/BVS/DFT method was utilized to elucidate the Li-ion transport system in  $\text{Li}_2\text{CoPO}_4\text{F}$ . Though VDP and BVS approaches identified a one-dimensional migration pathway along the [010] direction, taking into account lattice relaxation effects with the DFT-NEB method revealed additional low-barrier transitions, implying a three-dimensional migration. However, the electrode potentials attributed to the de/intercalation of more than one Li atom (>5.14 V vs  $\text{Li}/\text{Li}^+$ ), are out of the voltage stability range of the most of commercially available electrolytes, therefore, limiting the attainable specific capacity to 144 mAh/g or 1 Li atom per formula. In terms of energy density (~706 mWh/g for one Li per formula unit at an average potential of 4.9 V vs  $\text{Li}/\text{Li}^+$ ) and possibility of the 3D Li transport  $\text{Li}_2\text{CoPO}_4\text{F}$  can outperform  $\text{LiFePO}_4$  (580 mWh/g, 1D Li transport) and  $\text{LiVPO}_4\text{F}$  (650 mWh/g, 1D Li transport) cathodes. Thus, the material is still posing a challenge for researchers and engineers to unveil its full potential.

## ASSOCIATED CONTENT

### Supporting Information

The Supporting Information is available free of charge on the ACS Publications website at DOI: 10.1021/acs.jpcc.6b11027.

Details on DFT calculations and pDOS analysis for  $\text{Li}_{2-x}\text{CoPO}_4\text{F}$  (PDF)

Crystallographic parameters of  $\text{Li}_2\text{CoPO}_4\text{F}$  (CIF)

## AUTHOR INFORMATION

### Corresponding Author

\*S. S. Fedotov. E-mail: fedotov.msu@gmail.com.

### ORCID

Stanislav S. Fedotov: 0000-0003-4348-6517

Vladislav A. Blatov: 0000-0002-4048-7218

Andriy Zhugayevych: 0000-0003-4713-1289

### Author Contributions

The manuscript was written through contributions of all authors. All authors have given approval to the final version of the manuscript.

**Notes**

The authors declare no competing financial interest.

**ACKNOWLEDGMENTS**

This work was partly supported by Russian Science Foundation (S.S.F. and N.R.K. acknowledge grant #16-19-00190), Skoltech Center for Electrochemical Energy Storage and Moscow State University Development Program up to 2020. A.A.K., N.A.K. and V.A.B. thank the Russian Government (Grant 14.B25.31.0005). S.S.F. also acknowledges the Russian Foundation for Basic Research (RFBR, grant #16-33-00211 mol\_a) for purchasing experimental equipment, and Haldor Topsøe scholarship. The authors are grateful to E. A. Karpukhina (Moscow State University) for acquiring FTIR spectra, Dr. D. V. Sheptyakov (Paul Scherrer Institute, Villigen, Switzerland) for the technical support during neutron diffraction experiments, and Dr. D. A. Aksenen (Skoltech, CEE CREI) for helpful discussions on DFT methodology.

**REFERENCES**

- (1) Padhi, A. K.; Nanjundaswamy, K. S.; Goodenough, J. B. Phospho-Olivines as Positive-Electrode Materials for Rechargeable Lithium Batteries. *J. Electrochem. Soc.* **1997**, *144*, 1188–1194.
- (2) Goodenough, J. B.; Kim, Y. Challenges for Rechargeable Li Batteries. *Chem. Mater.* **2010**, *22*, 587–603.
- (3) Gutierrez, A.; Benedek, N. A.; Manthiram, A. Crystal-Chemical Guide for Understanding Redox Energy Variations of  $M^{2+/3+}$  Couples in Polyanion Cathodes for Lithium-Ion Batteries. *Chem. Mater.* **2013**, *25*, 4010–4016.
- (4) Okada, S.; Ueno, M.; Uebou, Y.; Yamaki, J. Fluoride Phosphate  $Li_2CoPO_4F$  as a High-Voltage Cathode in Li-Ion Batteries. *J. Power Sources* **2005**, *146*, 565–569.
- (5) Ellis, B. L.; Makahnouk, W. R. M.; Rowan-Weetaluktuk, W. N.; Ryan, D. H.; Nazar, L. F. Crystal Structure and Electrochemical Properties of  $A_2MPO_4F$  Fluorophosphates ( $A = Na, Li$ ;  $M = Fe, Mn, Co, Ni$ ). *Chem. Mater.* **2010**, *22*, 1059–1070.
- (6) Khasanova, N. R.; Gavrilov, A. N.; Antipov, E. V.; Bramnik, K. G.; Hibst, H. Structural Transformation of  $Li_2CoPO_4F$  upon Li-Deintercalation. *J. Power Sources* **2011**, *196*, 355–360.
- (7) Kim, S.-W.; Seo, D.-H.; Kim, H.; Park, K.-Y.; Kang, K. A. Comparative Study on  $Na_2MnPO_4F$  and  $Li_2MnPO_4F$  for Rechargeable Battery Cathodes. *Phys. Chem. Chem. Phys.* **2012**, *14*, 3299–3303.
- (8) Dutreilh, M.; Chevalier, C.; El-Ghazzi, M.; Avignant, D.; Montel, J. M. Synthesis and Crystal Structure of a New Lithium Nickel Fluorophosphate  $Li_2[NiF(PO_4)]$  with an Ordered Mixed Anionic Framework. *J. Solid State Chem.* **1999**, *142*, 1–5.
- (9) Ellis, B. L.; Makahnouk, W. R. M.; Makimura, Y.; Toghill, K.; Nazar, L. F. A Multifunctional 3.5 V Iron-Based Phosphate Cathode for Rechargeable Batteries. *Nat. Mater.* **2007**, *6*, 749–753.
- (10) Yakubovich, O. V.; Karimova, O. V.; Mel'nikov, O. K. The Mixed Anionic Framework in the Structure of  $Na_2\{MnF[PO_4]\}$ . *Acta Crystallogr., Sect. C: Cryst. Struct. Commun.* **1997**, *53*, 395–397 1997..
- (11) Dumont-Botto, E.; Bourbon, C.; Patoux, S.; Rozier, P.; Dolle, M. Synthesis by Spark Plasma Sintering: A New Way to Obtain Electrode Materials for Lithium Ion Batteries. *J. Power Sources* **2011**, *196*, 2274–2278.
- (12) Wang, D.; Xiao, J.; Xu, W.; Nie, Z.; Wang, C.; Graff, G.; Zhang, J.-G. Preparation and Electrochemical Investigation of  $Li_2CoPO_4F$  Cathode Material For Lithium-Ion Batteries. *J. Power Sources* **2011**, *196*, 2241–2245.
- (13) Wu, X.; Gong, Z.; Tan, S.; Yang, Y. Sol–Gel Synthesis of  $Li_2CoPO_4F/C$  Nanocomposite as a High Power Cathode Material for Lithium Ion Batteries. *J. Power Sources* **2012**, *220*, 122–129.
- (14) Khasanova, N. R.; Drozhzhin, O. A.; Fedotov, S. S.; Storozhilova, D. A.; Panin, R. V.; Antipov, E. V. Synthesis and Electrochemical Performance of  $Li_2Co_{1-x}M_xPO_4F$  ( $M = Fe, Mn$ ) Cathode Materials. *Beilstein J. Nanotechnol.* **2013**, *4*, 860–867.
- (15) Okumura, T.; Shikano, M.; Yamaguchi, Y.; Kobayashi, H. Structural Changes in  $Li_2CoPO_4F$  during Lithium-Ion Battery Reactions. *Chem. Mater.* **2015**, *27*, 2839–2847.
- (16) Amaresh, S.; Karthikeyan, K.; Kim, K. J.; Nahm, K. S.; Lee, Y. S. Alumina Coating on 5 V Lithium Cobalt Fluorophosphate Cathode Material for Lithium Secondary Batteries – Synthesis and Electrochemical Properties. *RSC Adv.* **2014**, *4*, 23107–23115.
- (17) Amaresh, S.; Karthikeyan, K.; Kim, K. J.; Kim, M. C.; Chung, K. Y.; Cho, B. W.; Lee, Y. S. Facile Synthesis of  $ZrO_2$  Coated  $Li_2CoPO_4F$  Cathode Materials for Lithium Secondary Batteries with Improved Electrochemical Properties. *J. Power Sources* **2013**, *244*, 395–402.
- (18) Wu, X.; Wang, S.; Lin, X.; Zhong, G.; Gong, Z.; Yang, Y. Promoting Long-Term Cycling Performance of High-Voltage  $Li_2CoPO_4F$  by the Stabilization of Electrode/Electrolyte Interface. *J. Mater. Chem. A* **2014**, *2*, 1006–1013.
- (19) Schoiber, J.; Berger, R. J. F.; Bernardi, J.; Schubert, M.; Yada, C.; Miki, H.; Hüsing, N. Straightforward Solvothermal Synthesis toward Phase Pure  $Li_2CoPO_4F$ . *Cryst. Growth Des.* **2016**, *16*, 4999–5005.
- (20) Ortiz, G. F.; López, M. C.; Li, Yixiao; McDonald, Matthew J.; Cabello, Marta; Tirado, José L.; Yang, Y. Enhancing the Energy Density of Safer Li-Ion Batteries by Combining High-Voltage Lithium Cobalt Fluorophosphate Cathodes and Nanostructured Titania Anodes. *Sci. Rep.* **2016**, *6*, 20656.
- (21) Lee, S.; Park, S. S. Lithium Transition Metal Fluorophosphates ( $Li_2CoPO_4F$  and  $Li_2NiPO_4F$ ) as Cathode Materials for Lithium Ion Battery from Atomistic Simulation. *J. Solid State Chem.* **2013**, *204*, 329–334.
- (22) Hadermann, J.; Abakumov, A. M.; Turner, S.; Hafideddine, Z.; Khasanova, N. R.; Antipov, E. V.; Van Tendeloo, G. Solving the Structure of Li Ion Battery Materials with Precession Electron Diffraction: Application to  $Li_2CoPO_4F$ . *Chem. Mater.* **2011**, *23*, 3540–3545.
- (23) Petricek, V.; Dusek, M.; Palatinus, L. Crystallographic Computing System JANA2006: General Features. *Z. Kristallogr. - Cryst. Mater.* **2014**, *229*, 345–352.
- (24) Blatov, V. A.; Shevchenko, A. P.; Proserpio, D. M. Applied Topological Analysis of Crystal Structures with the Program ToposPro. *Cryst. Growth Des.* **2014**, *14*, 3576–3586.
- (25) Anurova, N. A.; Blatov, V. A.; Ilyushin, G. D.; Blatova, O. A.; Ivanov-Schitz, A. K.; Dem'yanets, L. N. Migration Maps of  $Li^+$  Cations in Oxygen-Containing Compounds. *Solid State Ionics* **2008**, *179*, 2248–2254.
- (26) Blatov, V. A.; Shevchenko, A. P. Analysis of Voids in Crystal Structures: the Methods of Dual Crystal Chemistry. *Acta Crystallogr., Sect. A: Found. Crystallogr.* **2003**, *59*, 34–44.
- (27) Brown, I. D. Recent Developments in the Methods and Applications of the Bond Valence Model. *Chem. Rev.* **2009**, *109*, 6858–6919.
- (28) Sale, M.; Avdeev, M. 3DBVSMAPPER: a Program for Automatically Generating Bond-Valence Sum Landscapes. *J. Appl. Crystallogr.* **2012**, *45*, 1054–1056.
- (29) Hohenberg, P.; Kohn, W. Inhomogeneous Electron Gas. *Phys. Rev.* **1964**, *136*, B864–B871.
- (30) Henkelman, G.; Jónsson, H. Improved Tangent Estimate in the Nudged Elastic Band Method for Finding Minimum Energy Paths and Saddle Points. *J. Chem. Phys.* **2000**, *113*, 9978–9985.
- (31) Perdew, J. P.; Burke, K.; Ernzerhof, M. Generalized Gradient Approximation Made Simple. *Phys. Rev. Lett.* **1996**, *77*, 3865–3868.
- (32) Blochl, P. E. Projector Augmented-Wave Method. *Phys. Rev. B: Condens. Matter Mater. Phys.* **1994**, *50*, 17953–17979.
- (33) Kresse, G.; Furthmüller, J. Efficient Iterative Schemes for ab initio Total-Energy Calculations using a Plane-Wave Basis Set. *Phys. Rev. B: Condens. Matter Mater. Phys.* **1996**, *54*, 11169–11186.
- (34) Mueller, T.; Hautier, G.; Jain, A.; Ceder, G. Evaluation of Favorite-Structured Cathode Materials for Lithium-Ion Batteries using High-Throughput Computing. *Chem. Mater.* **2011**, *23*, 3854–3862.
- (35) Momma, K.; Izumi, F. VESTA 3 for Three-Dimensional Visualization of Crystal, Volumetric and Morphology Data. *J. Appl. Crystallogr.* **2011**, *44*, 1272–1276.

- (36) Dudarev, S. L.; Botton, G. A.; Savrasov, S. Y.; Humphreys, C. J.; Sutton, A. P. Electron-Energy-Loss Spectra and the Structural Stability of Nickel Oxide: An LSDA+U study. *Phys. Rev. B: Condens. Matter Mater. Phys.* **1998**, *57*, 1505–1509.
- (37) Urban, A.; Seo, D.-H.; Ceder, G. Computational Understanding of Li-ion Batteries. *npj Comput. Mater.* **2016**, *2*, 16002–16015.
- (38) Mueller, T.; Hautier, G.; Jain, A.; Ceder, G. Evaluation of Tavorite-Structured Cathode Materials for Lithium-Ion Batteries Using High-Throughput Computing. *Chem. Mater.* **2011**, *23*, 3854–3862.
- (39) Antipov, E. V.; Khasanova, N. R.; Fedotov, S. S. Perspectives on Li and Transition Metal Fluoride Phosphates as Cathode Materials for a New Generation of Li-ion Batteries. *IUCrJ* **2015**, *2*, 85–94.
- (40) Barpanda, P.; Oyama, G.; Nishimura, S.-i.; Chung, S.-C.; Yamada, A. A 3.8-V Earth-Abundant Sodium Battery Electrode. *Nat. Commun.* **2014**, *5*, 4358.
- (41) Yamada, A.; Chung, S. C.; Hinokuma, K. Optimized LiFePO<sub>4</sub> for Lithium Battery Cathodes. *J. Electrochem. Soc.* **2001**, *148*, A224–A229.
- (42) Ellis, B. L.; Ramesh, T. N.; Davis, L. J. M.; Goward, G. R.; Nazar, L. F. Structure and Electrochemistry of Two-Electron Redox Couples in Lithium Metal Fluorophosphates Based on the Tavorite Structure. *Chem. Mater.* **2011**, *23*, 5138–5148.
- (43) Karakulina, O. M.; Khasanova, N. R.; Drozhzhin, O. A.; Tsirlin, A. A.; Hadermann, J.; Antipov, E. V.; Abakumov, A. M. Antisite Disorder and Bond Valence Compensation in Li<sub>2</sub>FePO<sub>4</sub>F Cathode for Li-Ion Batteries. *Chem. Mater.* **2016**, *28*, 7578–7581.

SUPPORTING INFORMATION

## Crystal Structure and Li<sup>+</sup> Transport in Li<sub>2</sub>CoPO<sub>4</sub>F High-Voltage Cathode Material for Li-ion Batteries

Stanislav S. Fedotov<sup>†,‡,\*</sup>, Artem A. Kabanov<sup>§</sup>, Natalia A. Kabanova<sup>§</sup>, Vladislav A. Blatov<sup>§,#</sup>, Andriy Zhugayevych<sup>‡</sup>, Artem M. Abakumov<sup>‡,†</sup>, Nellie R. Khasanova<sup>†</sup>, Evgeny V. Antipov<sup>†</sup>

<sup>†</sup> Department of Chemistry, Lomonosov Moscow State University, Moscow 119991, Russia

<sup>‡</sup> Skoltech Center for Electrochemical Energy Storage, Skolkovo Institute of Science and Technology, Moscow 143026, Russia

<sup>§</sup> Samara Center for Theoretical Materials Science (SCTMS), Samara University, Samara 443011, Russia

<sup>#</sup> School of Materials Science and Engineering, Northwestern Polytechnical University, Xi'an, Shaanxi 710072, People's Republic of China

# $\text{Li}_{2-x}\text{CoPO}_4\text{F}$

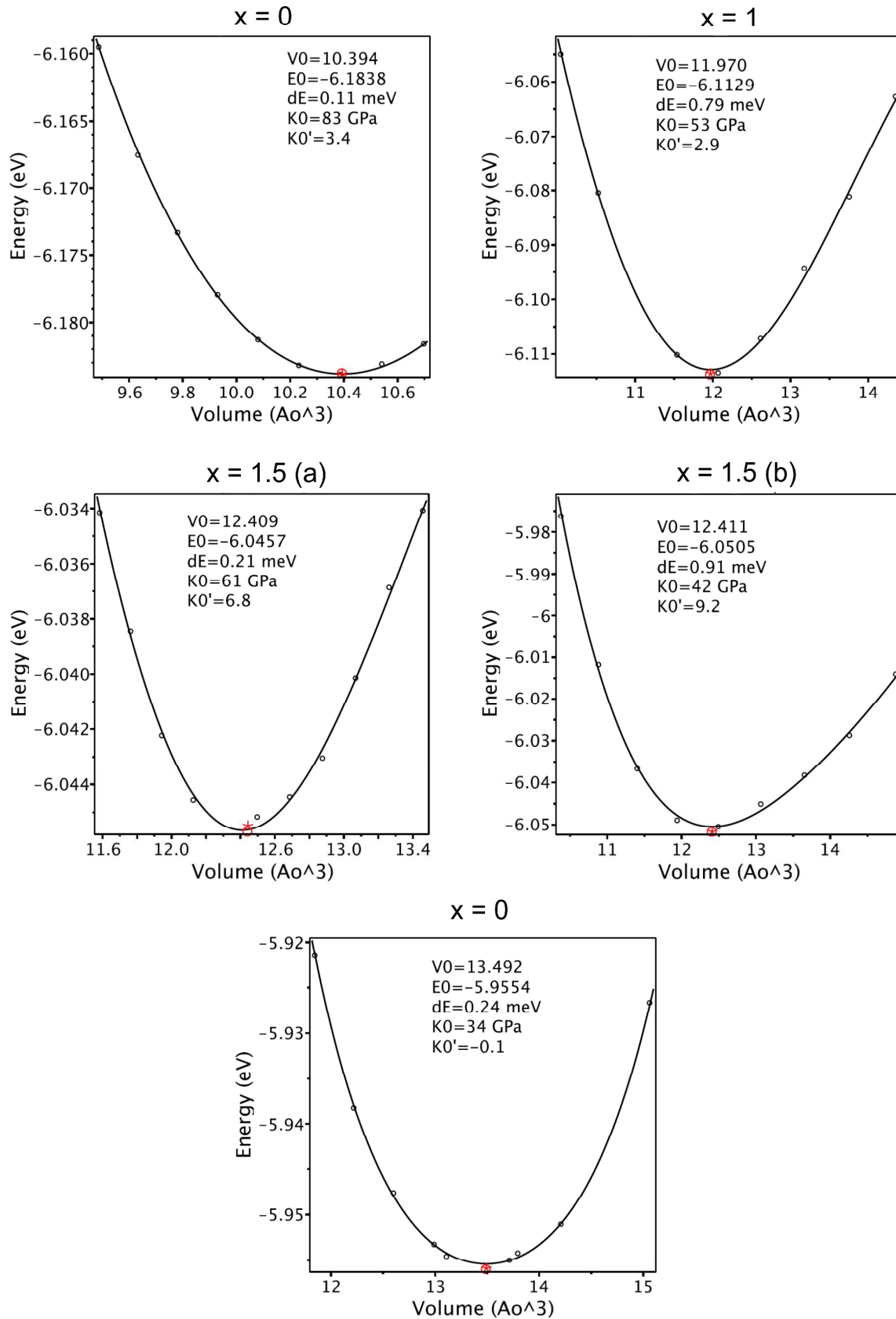


Figure S1. Volume scan for  $\text{Li}_{2-x}\text{CoPO}_4\text{F}$ .

# $\text{Li}_{2-x}\text{CoPO}_4\text{F}$

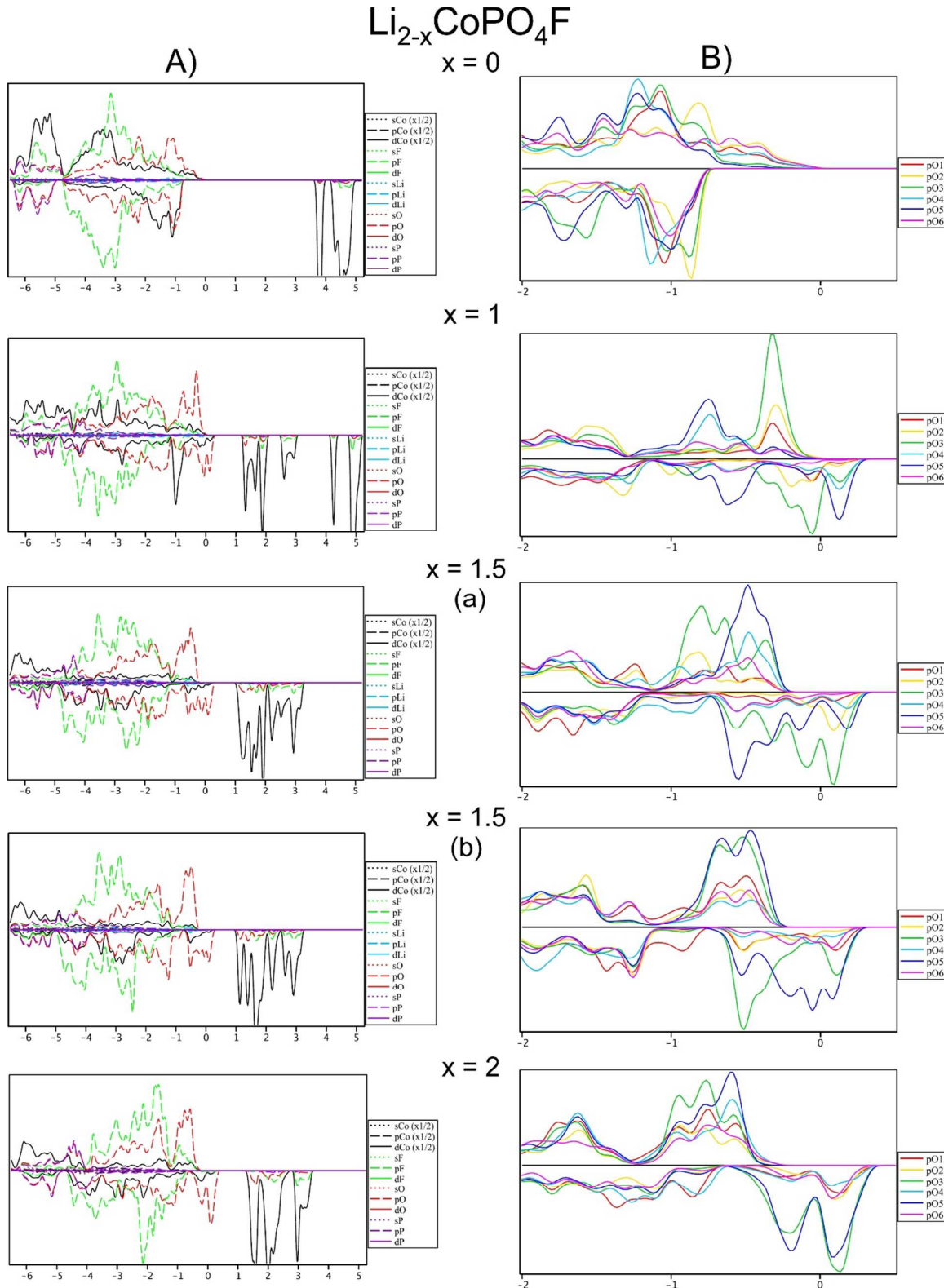


Figure S2. A) Partial Density of States (pDOS) for  $\text{Li}_{2-x}\text{CoPO}_4\text{F}$ , B) site resolved pDOS for different oxygen sites in  $\text{Li}_{2-x}\text{CoPO}_4\text{F}$ .